Retrieving the 3-D Tropospheric Wet Refractivity Field From a Standalone Ground-Based GNSS Station With A Priori Information: Theory and Simulation

Xianjie Li, Jingna Bai, Jean-Pierre Barriot, Yidong Lou, and Weixing Zhang

Abstract— Sensing water vapor contents in the troposphere with ground-based Global Navigation Satellite System (GNSS) stations has been widely studied and related to extreme weather events and climate changes over the years. Usually, GNSS tomography is the tool of choice to retrieve the 3-D water vapor field. However, a dense GNSS network is required, which means that the GNSS tomography is not applicable everywhere, e.g., in island countries, where only one/a few GNSS stations are available. In this work, we propose a new method to retrieve the 3-D wet refractivity field from the data collected at a standalone ground-based GNSS station. Using 3-D Zernike functions to model the turbulent component of the wet refractivity field and the corresponding perturbations in slant wet delays (SWDs), a typical Radon inverse problem is obtained. Two kinds of a priori information, namely, the spatial covariance of the SWDs and a Kaula-like rule, respectively, are proposed and introduced to regularize this ill-posed inverse problem. The proposed method is validated with a simulation experiment. The simulation results indicate its usefulness for retrieving the 3-D wet refractivity field overhead a single GNSS station with the appropriate a priori information.

Index Terms— 3-D Zernike functions, atmospheric turbulence, Global Navigation Satellite System (GNSS), Kaula-like rule, slant wet delay (SWD), Tikhonov regularization, wet refractivity field.

I. Introduction

THE Earth's atmosphere is rarely static but consists of ubiquitous nonturbulent and turbulent flows, particularly in the troposphere [1], [2]. As a result, variations of atmospheric variables in the troposphere, e.g., temperature, water vapor, and refractivity [3], could be found on various spatiotemporal scales (e.g., synoptic scale, mesoscale, and microscale) [4], [5]. These variations in water vapor contents make it difficult to determine or model the signal delays when radio-wave signals pass through the troposphere, i.e., the tropospheric delays [6]. Moreover, the variability of the water vapor content in the atmosphere is crucial by itself because it is inextricably linked to extreme weather events and climate changes [7].

The ground-based Global Navigation Satellite System (GNSS) is nowadays becoming one of the most promising techniques to continuously observe the water vapor content in the troposphere with the advent of GNSS meteorology [8], [9]. In convention, 1-D integrated amounts of water vapor (IWVs) can be obtained from the integrated tropospheric delays in GNSS signals, i.e., the slant wet delays (SWDs) and zenith wet delays (ZWDs). A 2-D ZWD/IWVs map is also available with a dense ground-based GNSS network (see [10], [11]). In terms of the 3-D distribution of the water vapor field, a lot of attention has been paid to GNSS tomography over the years (see [12], [13], [14], [15], [16], [17], [18], [19], [20]). However, a dense GNSS network is often required by GNSS tomography for collecting sufficient slant IWVs as input, which is too heavy to be implemented. This prerequisite restricts the application of GNSS tomography on a relatively small island where only a standalone GNSS station is available, e.g., Tahiti Island in French Polynesia with a diameter of about 30 km.

In this case, one may have other options for retrieving the 3-D water vapor field, such as the numerical weather models (NWMs) and water vapor differential absorption lidar (WVDIAL). Unfortunately, the resolution of the former is too low at present, e.g., the latest ERA5 now provides hourly products with a horizontal resolution of about 30 km [21], and it is still not economically feasible for the latter to build a network for observing the 3-D water vapor field [22]. To fill this gap, here in our study, we propose to apply a new model of the tropospheric delays, or more precisely, the SWDs, to retrieve the 3-D tropospheric wet refractivity field on a local scale overhead a standalone ground-based GNSS station. Here, the local scale is defined as a spatial scale ranging from several kilometers (2∼5 km) to hundreds of kilometers (∼100 km). The corresponding water vapor field could be inferred from the 3-D wet refractivity field since the refractivity is a function

of temperature, pressure, humidity, and electric density in the atmosphere [23]. Hence, we will hereinafter focus on the 3-D wet refractivity field.

Our new method follows the works by Barriot and Feng [4] and Barriot et al [24], where the wet refractivity field is represented by a well-recognized exponential decay together with a relatively small term ε_w reflecting the fluctuation/departure of the refractivity with respect to the exponential decay law. As proposed in [4], the term ε_w can be represented as a 3-D (or 4-D if the temporal evolution is concerned) series expansion based on a set of predefined orthogonal basis functions. By definition, the SWD is an integration of the wet refractivity along the ray path. Thereby, this integral relationship gives us a Radon transform [25]. Solving the 3-D wet refractivity field with SWDs is essentially a typical Radon inverse problem. Known as a classical ill-posed problem, this Radon inverse problem needs to be solved by applying some regularizations [26]. The truncated singular value decomposition (tSVD) method was used in the previous work by Barriot et al. [24]. However, some important features of the field may be lost due to truncation. A better way to obtain a physically acceptable solution is to introduce additional physical information about the observables or wet refractivity field from diverse sources [24]. Thereafter, this ill-posed problem can be solved with the Tikhonov regularization method as shown in the framework of radar tomography (see [27], [28]).

Therefore, in this work, we investigate the availability of the a priori information for reconstructing the 3-D wet refractivity field based on SWDs derived from a single GNSS station. Two kinds of appropriate a priori information are proposed and then adopted for a simulation study. The simulation and reconstruction form a closed-loop test to validate our proposed a priori information and the inverse process, which also reveals an alternative potential method for modeling and retrieving the 3-D wet refractivity field in the troposphere from a single GNSS station.

This article is organized as follows. To have a clear picture of the a priori information that is applicable to our study, possible a priori information related to SWDs and wet refractivity field in previous studies is revisited in Section II, leading to two kinds of proposed a priori information. The method that is used to model and simulate SWDs is introduced in Section III, where the adaptation of the a priori information proposed in Section II is elucidated. The inverse process is also given in this section with details. In Section IV, the experimental results of the simulation and reconstruction are presented and discussed. Finally, our conclusion is given in Section V.

II. REVISIT OF THE A PRIORI INFORMATION FOR REGULARIZATIONS

The concept of introducing the a priori information of parameters or observations in data analysis is not new in the space geodesy community, e.g., the a priori empirical elevation-dependent weighted matrix for observations in GNSS data processing. Here, in our work, specifically, by the a priori information, we mean the temporal or spatial correlation/(co)variance function of the quantity that is of concern, i.e., SWDs or wet refractivity.

One possible way to obtain such a priori information is from atmospheric turbulence theory [29], [30]. By assuming a statistically homogeneous and isotropic turbulent atmosphere, the covariance function of the wet refractive index can be directly computed from the refractive index structure function that follows the well-known 2/3 Kolmogorov scaling law (see [31], [32]). These turbulence-based covariance functions of wet refractive index were successfully introduced as the a priori information in the Kalman filter of GPS tomography for simulation studies, see [33], [34].

Moreover, the (co)variance function of SWDs can be derived from the (co)variance matrix of phase observations in space geodesy if one assumes that the correlations between them are predominantly introduced by isotropic turbulence occupying a "slab" boundary layer (typically below 1–2 km altitude). Pioneering work in terms of correlations in very long baseline interferometry (VLBI) observations can be found in [35] (or the TL model). Similarly, using the spectral representation of atmospheric turbulence, Schön and Brunner [36] proposed a generalized form of the TL model. Both methods were then adopted and verified in many other applications in space geodesy with both real datasets and simulations (see [5], [6], [37], [38], [39], [40], [41], [42]) as it has been shown to improve the quality and precision description of parameter estimations. However, all the above covariance functions are derived based on turbulence models, the parameters of which are given empirically and are only approximations to the truth. One needs to be cautious when applying these covariance functions since the assumptions that these turbulent models underlie may no longer be valid in real cases.

On the other hand, according to the conventional model of SWDs in GNSS data processing with mapping functions and horizontal gradients, statistical information on ZWDs or horizontal gradients could also give us indications for the covariance function of SWDs. Indeed, the variations of GNSS-derived ZWD/IWV on different time scales have been analyzed both in meteorological (see [43], [44], [45], [46], and references therein) and climatological studies (see [8], [11], [47], [48], and references therein) over the years. Horizontal gradients were also found to help describe the anisotropy of the water vapor field and detect small-scale convective structures as a valuable indicator (e.g., [49], [50], [51], [52]). Nevertheless, the temporal or spatial variations of ZWD/IWV before and after the onset of severe weather events are the main target of previous literature dealing with severe weather events [46]. Only temporal variations of the 1-D IWV are analyzed, which cannot represent the 3-D nature of the water vapor field [44]. A similar problem can be found in climate research with GNSS as the studies so far have been limited to investigating the long-term linear trends in IWVs [45].

Another alternative way is to derive the covariance function from the statistical property of the SWDs or wet refractivity field sampled over NWMs on various spatiotemporal scales. Again, as we mentioned before, the spatial resolution of NWMs at present is too low to be applied to our case.

In summary, the covariance function of SWDs or the wet refractivity that we are looking for should describe their correlations within a relatively small spatial scale (tens of

kilometers) but with various time scales (ranging from minutes to weeks). This means that both atmospheric turbulent and nonturbulent flows on the microscale, mesoscale, and even the synoptic scale are concerned in our case. The impacts of these atmospheric flows on the covariance function of SWDs or the refractivity field hence should be considered.

Fortunately, Zhang et al. [53] recently found a covariance function of SWDs that applies to our case. Based on real datasets collected at one GNSS station for about eight months, Zhang et al. [53] presented the statistical property of an almost stationary process with respect to the elevation angle el, i.e., $SE = SWD \cdot \sin(el)$. This approach was first used in previous studies of the SWDs, e.g., [40], [54]. In Zhang et al.'s work [53], this SE series was expanded with spherical harmonics in space and trigonometric functions in time. Thereby, an angular correlation length of about 20° and a correlation time of up to four days are reported. Here, in this work, we will adopt this spatial covariance information as the a priori information for SWDs or, strictly speaking, SEs.

It is worth noting that an additional a priori information (or constraint) needs to be introduced, which is implicitly suggested in our model of ε_w. Since we assume that the term ε_w can be modeled by a set of orthogonal, "well-behaved" functions, staying within certain bounds, the parameters of functions generally should decrease in magnitude as the degrees of functions increase according to Parseval's theorem [55], [56]. Such a constraint is widely used in modeling the gravitational and geopotential field of the Earth with spherical harmonics (see [57], [58], [59], [60]), which is known as Kaula's rule [55], [61]. This rule of thumb states that the degree variance of normalized harmonic parameters is proportional to the inverse cube of the degree l, i.e., $\sim 10^{-10}/l^3$ [55]. Considering that spherical harmonics are included in our model (see Section III) and the similarity in inversion studies between the atmospheric refractivity field and the geopotential field, it is natural to come to a hypothesis that a similar Kaula's rule taking the power-law form will provide the a priori constraint for our model parameters. However, this Kaula-type power rule needs to be slightly adapted to our case, which will be discussed in detail in Section III-B.

III. METHODOLOGY

A. Modelization

A good approximation of refractive index $n(r)$ in the troposphere can be taken as a twofold exponential formula [4]

$$n(r) = 1 + N_h + N_w$$
$$= 1 + N_h^0 \cdot \exp\left(-\frac{r - r_0}{H_h}\right) + N_w^0 \cdot \exp\left(-\frac{r - r_0}{H_w}\right) \quad (1)$$

where N_h is the hydrostatic refractivity; N_w is the wet refractivity; r is the geocentric radius; r_0 is the geocentric radius at the GNSS receiver; N_h^0 and N_w^0 are the hydrostatic and wet refractivity at the receiver, respectively; H_h is the scale height of N_h; and H_w is the scale height of N_w, also known as water vapor scale height. Since delays caused by the hydrostatic component (i.e., N_h) can be accurately determined by a model with atmospheric pressure measurements, see [62], we here

only focus on N_w, which is highly variable both in time and space due to the highly variable water vapor content in the troposphere [63].

Taking into account both the nonturbulent and turbulent flows in the troposphere, the wet refractivity field can be represented as [4], [24]

$$N_w = N_w^0 \cdot \exp\left(-\frac{r - r_0}{H_w}\right) \cdot (1 + \varepsilon_w(x, y, z, t)) \quad (2)$$

where a relatively small term ε_w ($|\varepsilon_w| \ll 1$) is introduced to represent the fluctuation/departure of the refractivity with respect to the general exponential decay law; x, y, and z are spatial coordinates in a given frame; and t denotes the time. As proposed in [4], the term ε_w in (2) can be represented as a 4-D series expansion with a set of predefined orthogonal basis functions. Here, in our case, we adopt a set of orthonormal functions with respect to time $T_u(t)$ up to degree $u_{\max}$ to describe the variations of ε_w in time and 3-D Zernike functions up to degree $n_{\max}$ to express ε_w in space with the spherical coordinate as

$$\varepsilon_w(x, y, z, t) = \varepsilon_w(r, \theta, \lambda, t)$$
$$= \sum_{u=0}^{u_{\max}} \sum_{n=0}^{n_{\max}} \sum_{l=0}^{n} \sum_{m=0}^{l} T_u(t) R_n^l(r) Y_l^m(\theta, \lambda) p_{nl,u}^m$$
$$(3)$$

where radial polynomials $R_n^l(r)$ ($0 \leq r \leq 1$) and spherical harmonics $Y_l^m(\theta, \lambda)$ form a set of orthonormal basis functions over a whole ball (i.e., the 3-D Zernike functions) with r, θ, and λ denoting the radial distance, polar angle, and azimuthal angle in the spherical coordinate, respectively. Here, u, n, m, and l are integers with $u \geq 0$, $0 \leq l \leq n$, $0 \leq m \leq l$, $n - l$ is even, and $m + l$ is even for orthogonality over the hemisphere. $p_{nl,u}^m$ are the parameters in the model to be estimated. The definition of 3-D Zernike functions is highly technical, we therefore refer to [64], [65], and [66] for further details.

Although the 4-D wet refractivity field is of more concern, taking the temporal variations into account will introduce a high degree of freedom in the model, which is too complicated to deal with at the moment. At this stage, we only consider the 3-D wet refractivity field, i.e., the wet refractivity field overhead a standalone GNSS station at a fixed measurement epoch [i.e., $t = t_F$ and $T_u(t_F) = 1$]. The 4-D case with time t involved will be investigated in our future work. Hence, the term t in ε_w is removed from (2) and (3) in this work as

$$\varepsilon_w(x, y, z) = \varepsilon_w(r, \theta, \lambda) = \sum_{n=0}^{n_{\max}} \sum_{l=0}^{n} \sum_{m=0}^{l} R_n^l(r) Y_l^m(\theta, \lambda) p_{nl}^m.$$
$$(4)$$

For simplicity, we hereinafter use a matrix representation of the model

$$\boldsymbol{\varepsilon}_w = \boldsymbol{G}_w \cdot \boldsymbol{p} \quad (5)$$

with $\boldsymbol{G}_w$ and $\boldsymbol{p}$ representing the matrix of coefficients $R_n^l(r) Y_l^m(\theta, \lambda)$ and the vector of parameters p_{nl}^m in (4), respectively.

By definition, the SWD is an integration of the wet refractivity along the ray path S launching at elevation angle el and azimuth angle λ, which reads

$$\text{SWD}(el, \lambda) = \int_{S(el,\lambda)} N_w^0 \cdot \exp\left(-\frac{r - r_0}{H_w}\right) \cdot (1 + \varepsilon_w) ds. \tag{6}$$

According to the ansatz [24]

$$\int \exp(-a\mu) \cdot \mu^c d\mu = -\frac{1}{a^{c+1}} \Gamma(c + 1, a\mu). \tag{7}$$

Equation (6) can be further expanded as

$$\text{SWD}(el, \lambda) = \overline{\text{SWD}}(el, \lambda) + \delta\text{SWD}(el, \lambda) \tag{8}$$

where

$$\overline{\text{SWD}}(el, \lambda) = -\frac{N_w^0 H_w}{\sin(el)} \left(\exp\left(-\frac{S \cdot \sin(el)}{H_w}\right) - 1\right) \tag{9}$$

and

$$\begin{aligned}
&\delta\text{SWD}(el, \lambda) \\
&= N_w^0 S \\
&\cdot \sum_{n=0}^{n_{\max}} \sum_{l=0}^{n} \sum_{m=0}^{l} \left[\sum_{v=0}^{k} q_{kl}^v \cdot \gamma(2v + l + 1, a) \cdot a^{-(2v+l)-1}\right] \\
&\cdot Y_l^m\left(\frac{\pi}{2} - el, \lambda\right) \cdot p_{nl}^m.
\end{aligned} \tag{10}$$

We assume that the ray path is limited to a certain azimuthally fixed vertical plane. Here, q_{kl}^v are the coefficients in the radial polynomials $R_n^l(r)$ with integer v taking values from 0 to $k = (n - l)/2$ and $a = S \cdot \sin(el)/H_w$, where S is the ray path length, H_w is the water vapor scale height, μ represents the first moment of 3-D Zernike functions, and γ denotes the lower incomplete Gamma function. Further derivations of (8)–(10) can be found in the Appendix. In analogy, once SWDs at various elevation and azimuth angles are obtained, one can rewrite (8) into its matrix form

$$\boldsymbol{SWD} = \overline{\boldsymbol{SWD}} + \boldsymbol{G_I} \cdot \boldsymbol{p}. \tag{11}$$

The so-called SE is simply a production of SWDs and the sine function of the corresponding elevation angles el as [53]

$$\text{SE}(el, \lambda) = \text{SWD}(el, \lambda) \cdot \sin(el) \tag{12}$$

of which the matrix form reads

$$\boldsymbol{SE} = \overline{\boldsymbol{SE}} + \boldsymbol{G} \cdot \boldsymbol{p}. \tag{13}$$

B. A Priori Information

As aforementioned, the a priori information given by Zhang et al. [53] is adopted in our simulation study. The temporal evolution is not taken into account at this moment, and therefore, only the spatial covariance function of the SEs with an angular correlation length of about $20°$ is used here. To put it simply, we approximate this spatial covariance function in an analytical form as

$$\text{Cov}_{\text{SE}}(\Psi) = \delta_0^2 \cdot \exp\left(-(\Psi/20)^2\right) \tag{14}$$

where Ψ is the spherical distance in degree and δ_0^2 is the variance. We will hereafter use $\boldsymbol{Cov}_{\text{SE}}$ denoting the covariance function in its matrix form.

An additional constraint for parameters $\boldsymbol{p}$ needs to be introduced according to Parseval's theorem. Taking Kaula's rule as a prototype, we here propose a Kaula-like rule for the variance of parameters $\boldsymbol{p}$ in our case as

$$\delta_{nl}^2 = \sum_m \left|p_{nl}^m\right|^2 = \frac{A}{n^\alpha p^\beta} \tag{15}$$

considering that both degrees n and l in 3-D Zernike functions have physical significance. Order m is not considered as it has no physical significance in the degree variance of spherical harmonics. Here, $A > 0$ is an empirical constant, and $\alpha > 0$ and $\beta > 0$ are the power of degrees n and l, respectively.

In practice, following the derivation of Kaula's rule [61], one possible method to determine the unknowns in (15) (i.e., A, α, and β) is from a spectral analysis of the wet refractivity field over the spatial and time scale that is of concern, e.g., from NWM products. Unfortunately, it is not applicable in our case due to the low resolution of the present NWM products. Nevertheless, a good indication for the values of $\alpha = 2$ and $\beta = 2$ can be found in previous studies related to the spectral behavior of wind speed or other atmospheric variables (see [67], [68], [69], and references therein). The determination of the constant A is case-dependent. In this way, the a priori constraint with a diagonal (co)variance matrix $\boldsymbol{C_p}$ for parameters $\boldsymbol{p}$ can be obtained from (15).

Provided that $\boldsymbol{Cov}_{\text{SE}}$ and $\boldsymbol{C_p}$ for parameters $\boldsymbol{p}$ are available, the a priori information of parameters $\boldsymbol{p}$ can be derived as [70], [71]

$$\boldsymbol{Cov_p} = \left(\boldsymbol{G}^{\mathrm{T}}\boldsymbol{G} + \boldsymbol{C_p}^{-1}\right)^{-1} \boldsymbol{G}^{\mathrm{T}} \boldsymbol{Cov}_{\text{SE}} \boldsymbol{G} \left(\boldsymbol{G}^{\mathrm{T}}\boldsymbol{G} + \boldsymbol{C_p}^{-1}\right)^{-1} \tag{16}$$

recalling the model of SEs in (13).

C. Simulation

The a priori information of parameters $\boldsymbol{p}$, i.e., $\boldsymbol{Cov_p}$ in (16), allows us to simulate a set of Gaussian random parameters $\boldsymbol{p}$, as well as the SE series. This can be done with the spectral decomposition approach [72]. In this approach, the SVD of $\boldsymbol{Cov_p}$ is first implemented to obtain the orthonormal matrix of eigenvectors $\boldsymbol{V}$ and eigenvalues $\boldsymbol{\Lambda}$ as

$$\boldsymbol{Cov_p} = \boldsymbol{V} \cdot \boldsymbol{\Lambda} \cdot \boldsymbol{V}^{\mathrm{T}}. \tag{17}$$

Thereafter, a set of parameters $\boldsymbol{p}^s$ can be simulated by

$$\boldsymbol{p}^s = \boldsymbol{V} \cdot \sqrt{\boldsymbol{\Lambda}} \cdot \boldsymbol{w} \tag{18}$$

with a vector of random variables $\boldsymbol{w} = [w_1, w_2, \ldots]$ taking Gaussian normal distribution with mean 0 and variance 1. In this way, the simulated parameters $\boldsymbol{p}^s$ will take zero mean and (co)variance $\boldsymbol{Cov_p}$.

Recalling the model of SEs in (13), a set of SE series could also be generated based on the simulated parameters $\boldsymbol{p}^s$ as

$$\boldsymbol{SE}^s = \overline{\boldsymbol{SE}^s} + \boldsymbol{G} \cdot \boldsymbol{p}^s. \tag{19}$$

D. Inverse Process

Taking the simulated SE^s as input, let us now consider the linear inverse problem given in (13). The inverse problem is endogenously ill-posed because the input signals/observations are integrated values, e.g., SE/SWDs. To obtain a reasonable and stable solution, here in our case, we propose to introduce the derived a priori covariance matrix of parameters Cov_p for the regularization of the ill-posed inverse problem. Under the principle of least square, this ill-posed linear inverse problem can then be solved following the so-called Tikhonov regularization method [71], [73] as

$$\widehat{p}^s = \left(G^{\mathrm{T}}G + \chi \cdot Cov_p^{-1}\right)^{-1}G^{\mathrm{T}}\left(SE^s - \overline{SE}^s\right) \qquad (20)$$

where $\chi > 0$ is a regularization parameter that indicates the weighting of the additional a priori information in the inverse process.

Several different strategies can be applied to choose this regularization parameter χ (see [73] and references therein), e.g., making a compromise between the norm of the residuals and the norm of the solution. However, no "best" strategy exists as it depends on the application. Instead, a pragmatic one is more practical.

Thereafter, we can reconstruct the SE series with (13) as

$$\widehat{SE}^s = \overline{SE}^s + G \cdot \widehat{p}^s \qquad (21)$$

and also, the wet refractivity field in (2) with

$$\widehat{\varepsilon_w} = G_w \cdot \widehat{p}^s \qquad (22)$$

based on (5).

IV. SIMULATIONS AND EXPERIMENT RESULTS

A. Simulation Setup

As a rule of thumb, a single ground-based GNSS station can observe water vapor information of about a 100-km radius in the horizontal direction (with a cutoff elevation angle of 10°) [8]. Taking a single GNSS station located on Tahiti Island as a prototype, the typical height of the tropopause is 16.5 km in this tropical region. Therefore, in our simulation, a 3-D refractivity field with a horizontal scale of 200×200 km and a vertical scale of up to 16.5 km high is considered. Some simulation parameters are fixed to constants, such as the Earth's radius $r_0 = 6371$ km, $N_w^0 = 128 \cdot 10^{-6}$, and the water vapor scale height $H_w = 2.391$ km according to [24], and the other parameters will be determined in the following case-dependent analysis.

To give a good spatial representation of the field, the SWD/SEs are simulated at random elevation and azimuth angles on the hemisphere over the single station. A cutoff elevation angle of 10° is chosen to avoid the anomalies near the horizon since no observations below the horizon are available in reality to constrain the function behavior. Finally, 4148 SWD/SEs over the hemisphere were sampled and simulated in this experiment and their distribution is given in Fig. 1. Note that in real cases, the distribution of SWDs overhead a standalone GNSS station is much sparser with periodic GNSS satellite tracks.
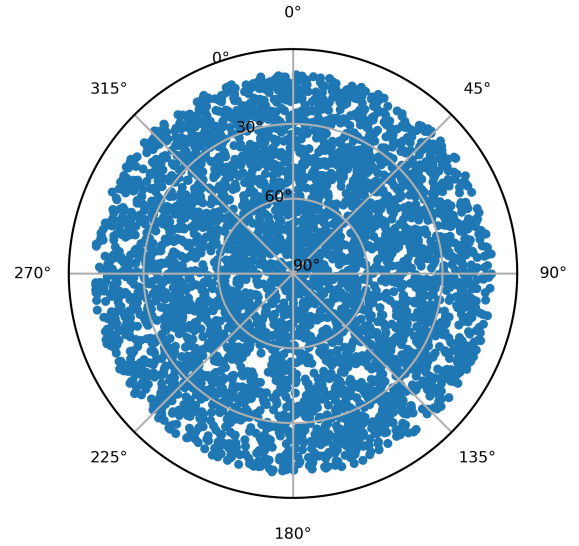

Fig. 1. Sky plot of the spatial distribution of the simulated SWD/SEs over a single GNSS station with a cutoff elevation angle of 10°.
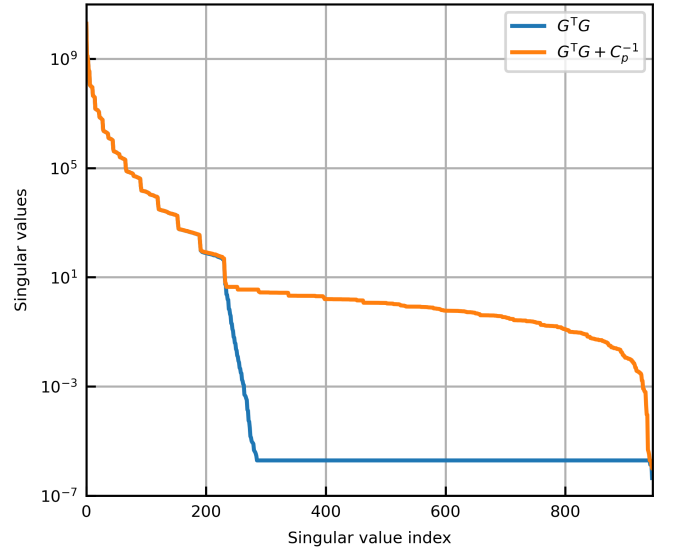

Fig. 2. Log10 plots of singular values of $G^{\mathrm{T}}G$ (blue) and $G^{\mathrm{T}}G + C_p^{-1}$ with $A = 2.5 \times 10^4$ (orange).

Based on the spatial distribution in Fig. 1 and using (14), Cov_{SE} is generated. The variance δ_0^2 is regulated to 10 to ensure that the variations of the simulated SEs are in a physically reasonable range, i.e., about 305 ± 10 mm in our case. By adopting the model with 3-D Zernike functions up to degree 20 (i.e., $n_{\max} = 20$), we generate the design matrix G for SEs based on the setup of elevation and azimuth angles above. The number of unknown parameters is 946.

After several trials with different A's in (15) to derive Cov_p, we found that A significantly affects relatively small singular values of $G^{\mathrm{T}}G + C_p^{-1}$ in (16). We decided to take a value of A by visual inspection of the decrease pattern of singular values, as shown in Fig. 2. Taking $A = 2.5 \times 10^4$, we are able to keep all the relatively large singular values as those in $G^{\mathrm{T}}G$ and suppress the sharp decrease in smaller singular values of $G^{\mathrm{T}}G$.

However, even with the addition of the diagonal matrix C_p^{-1}, the matrix $G^{\mathrm{T}}G + C_p^{-1}$ is not guaranteed to be numerically

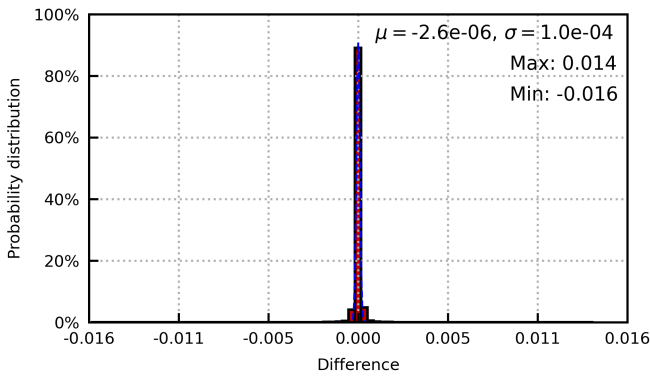Fig. 3.   Statistical histogram distribution of the differences between the original and reconstructed matrix $\boldsymbol{G}^{\mathrm{T}}\boldsymbol{G} + \boldsymbol{C}_{\boldsymbol{p}}^{-1}$ with tSVD.
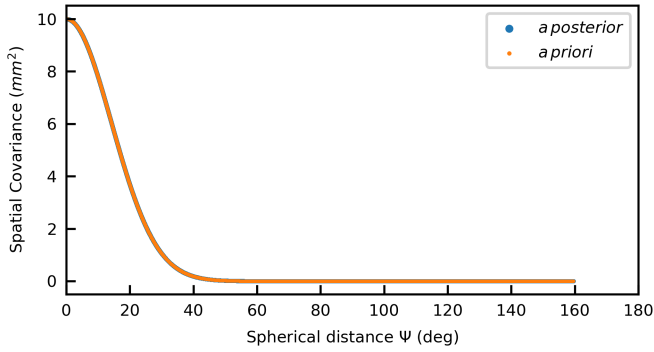

Fig. 4.   Covariance functions of SEs with respect to the spherical distances Ψ. The generated a priori covariance function is shown in orange dots and the a posteriori covariance function is given in blue dots.
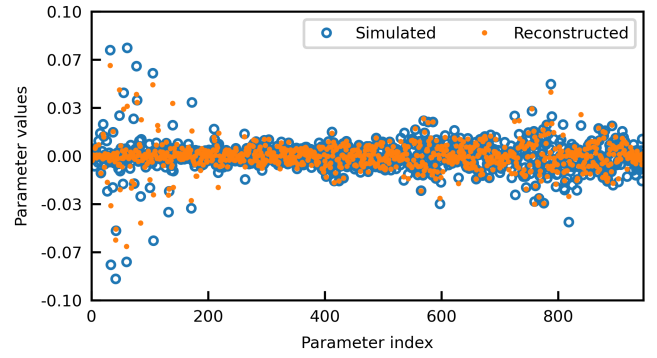

Fig. 5.   Series of the simulated parameters (blue circles) and reconstructed parameters (orange dots).
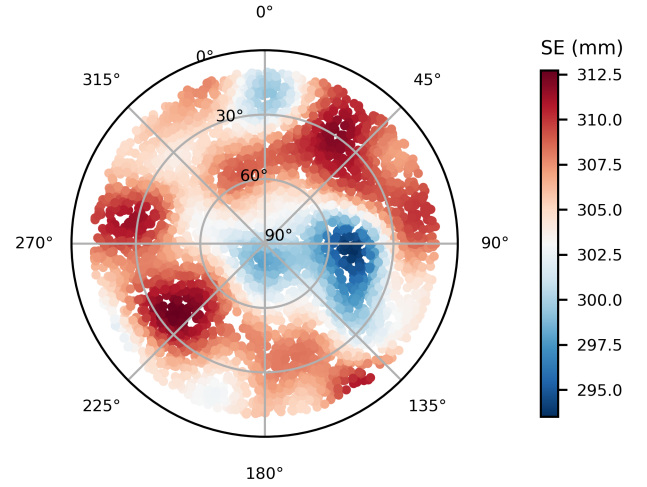

Fig. 6.   Sky plot of the simulated SEs over the hemisphere from the viewpoint of a single GNSS station.
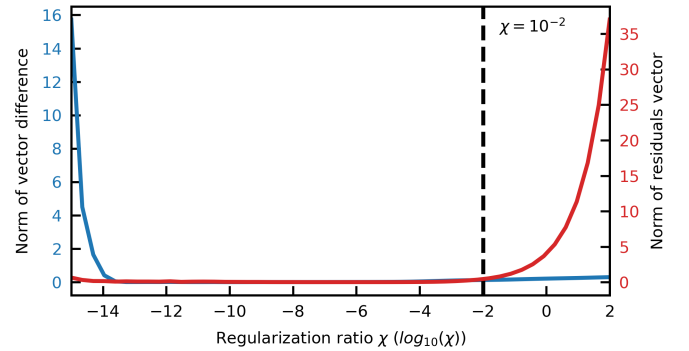

Fig. 7.   Choice of the regularization parameter χ by achieving a compromise between the norm of the residual vector and the norm of the vector difference of the reconstructed solution and the true solution.

invertible. Here, in our case, we use the tSVD method to get an approximation of the inverse of matrix $\boldsymbol{G}^{\mathrm{T}}\boldsymbol{G} + \boldsymbol{C}_{\boldsymbol{p}}^{-1}$. By truncating the 900 leading singular values, the truncated matrix still retains the major characteristics of $\boldsymbol{G}^{\mathrm{T}}\boldsymbol{G} + \boldsymbol{C}_{\boldsymbol{p}}^{-1}$, e.g., the norm of the truncated matrix takes over 99.9% of the original $\boldsymbol{G}^{\mathrm{T}}\boldsymbol{G} + \boldsymbol{C}_{\boldsymbol{p}}^{-1}$. This is also indicated in Fig. 3, where the statistical histogram distribution of the differences between them is shown. Only a small fraction of information is lost due to the truncation.

To further validate the approximated $(\boldsymbol{G}^{\mathrm{T}}\boldsymbol{G} + \boldsymbol{C}_{\boldsymbol{p}}^{-1})^{-1}$ from tSVD, a comparison between the generated $\boldsymbol{Cov}_{\mathrm{SE}}$ and the a posteriori $\boldsymbol{Cov}'_{\mathrm{SE}}$ is shown in Fig. 4, of which $\boldsymbol{Cov}'_{\mathrm{SE}} = \boldsymbol{G}\boldsymbol{Cov}_{\mathrm{SE}}\boldsymbol{G}^{\mathrm{T}}$ is derived according to the error propagation law. A good agreement can be found in the figure as the norm of $\boldsymbol{Cov}_{\mathrm{SE}}$ takes over 99.9% of the norm of $\boldsymbol{Cov}'_{\mathrm{SE}}$.

B. Experimental Results

With $\boldsymbol{Cov}_{\boldsymbol{p}}$ derived from (16), a set of Gaussian random parameters $\boldsymbol{p}^s$ is simulated by applying the spectral decomposition with (17) and (18), as shown in Fig. 5. The corresponding $\boldsymbol{SE}^s$ values are then generated using (19) (see Fig. 6), where the computation of the mean part $\overline{\boldsymbol{SE}^s}$ can be found in the Appendix with (12).

Taking the simulated SEs as input, the ill-posed inverse problem in (13) can be solved with the Tikhonov regularization method as given in (20). Since the "true" values of parameters are known in our simulation, we selected $\chi = 0.01$ to make a

compromise between the norm of the residuals vector and the norm of the vector difference of the reconstructed solution and the true solution (see Fig. 7). However, in real cases, a better way to determine χ is to compare the reconstructed refractivity field with those observed/derived from other techniques, such as the vertical profile of refractivity derived from radiosonde.

The reconstructed parameters $\hat{\boldsymbol{p}}_s$ are shown in Fig. 5 together with the simulated $\boldsymbol{p}^s$. Residuals of the reconstructed SEs are shown in Fig. 8. Overall, the reconstructed parameters agree well with the simulated ones and a good agreement
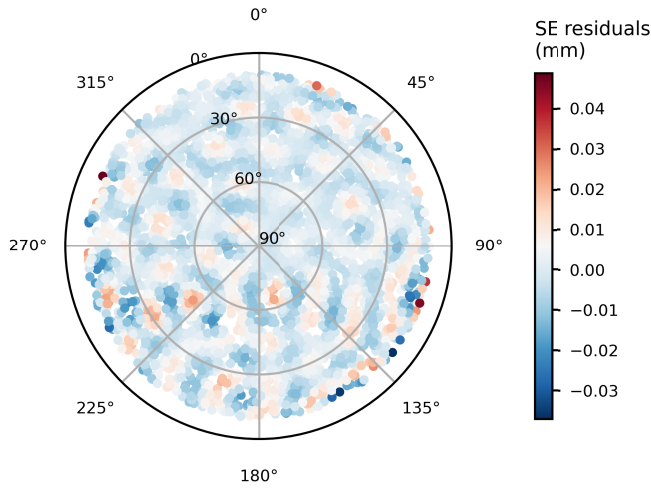
Fig. 8. Sky plot of the residuals of the reconstructed SEs compared to the simulated ones.
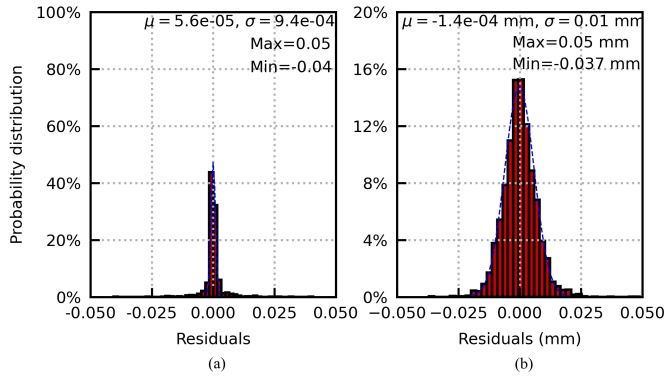

Fig. 9. Statistical histogram distributions of the residuals of (a) reconstructed parameters p^s and (b) reconstructed SE^s.

could also be found between $\widehat{SE^s}$ and SE^s. These results are validated in the corresponding statistical histograms of the residuals given in Fig. 9. More specifically, the mean of the SE residuals is about -1.4×10^{-4} mm and the root mean square (rms) takes about 0.01 mm. The minimum and maximum SE residuals are about -0.037 and 0.05 mm, respectively. Most of the relatively large SE residuals are found at low elevation angles, which may be ascribed to the less constrained behavior of our model near the boundary of the simulated observations geometry.

Finally, the 3-D wet refractivity field is retrieved according to (22) and (2). The 2-D profiles of the simulated and reconstructed fluctuating component ε_w in the north–south direction (azimuth angles 0° and 180°) are shown and compared in Fig. 10. Taking the exponential decay into account, the corresponding 2-D profiles of the simulated and reconstructed 3-D wet refractivity field in the north–south direction are presented in Fig. 11. An overall good agreement between them can be concluded.

A full picture of the 3-D distribution of the simulated and reconstructed ε_w, as well as the wet refractivity field, is presented in Figs. 12 and 13 and Figs. 14 and 15, respectively. Note that all the 3-D plots are presented in the topocentric cartesian coordinate of the single GNSS station. Turbulent
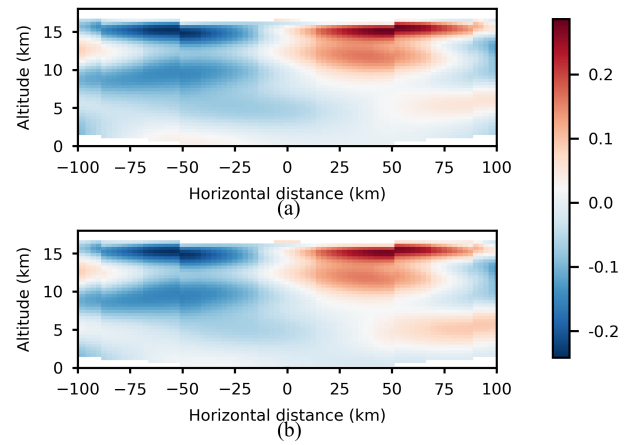

Fig. 10. Two-dimensional profiles of (a) simulated and (b) reconstructed fluctuating component of the 3-D wet refractivity field in the north–south direction.
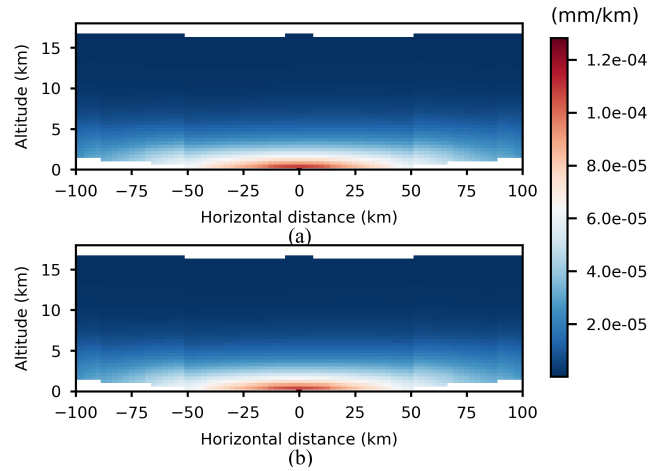

Fig. 11. Two-dimensional profiles of (a) simulated and (b) reconstructed 3-D wet refractivity field in the north–south direction.
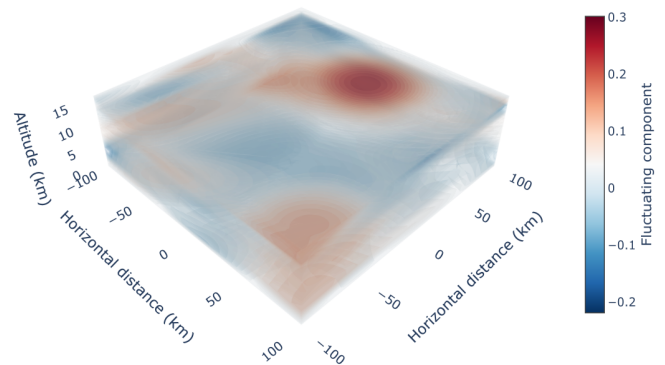

Fig. 12. Three-dimensional distribution of the fluctuating component ε_w of the simulated wet refractivity field.

eddies can be found not only in 2-D profiles but also in the 3-D distribution of the wet refractivity field overhead the single GNSS station (see Figs. 10, 12, and 13). However, the impacts of these turbulent eddies are relatively small and decayed associated with the exponential decay of the wet refractivity with respect to the altitude. Therefore, no apparent fluctuations
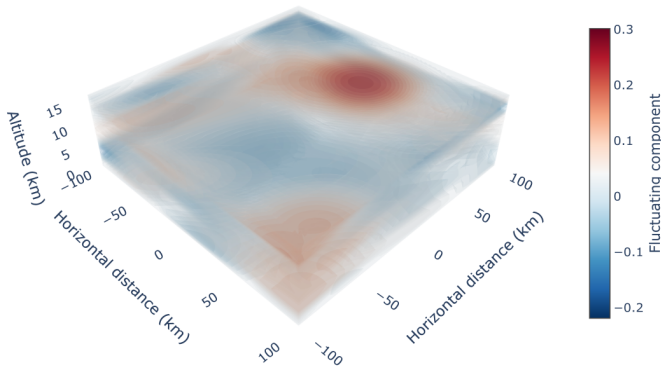
Fig. 13. Three-dimensional distribution of the fluctuating component ε_w of the reconstructed wet refractivity field.
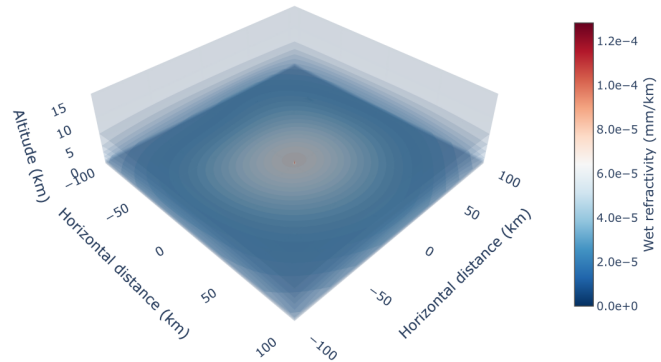

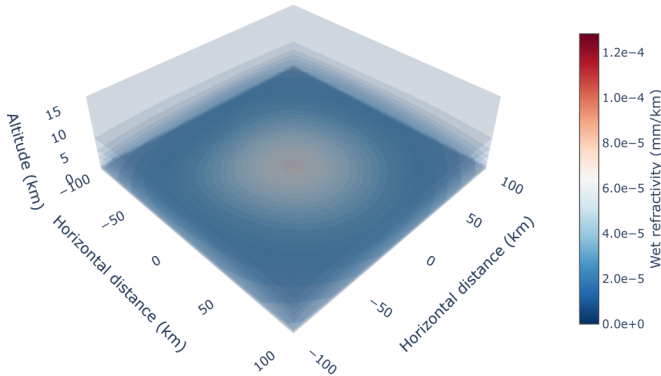Fig. 14. Three-dimensional distribution of the simulated wet refractivity field.

Fig. 15. Three-dimensional distribution of the reconstructed wet refractivity field.

are shown in the 3-D wet refractivity field (see Figs. 11, 14, and 15).

V. CONCLUSION

We have presented a new potential function-based method for retrieving the 3-D wet refractivity field overhead from the SWDs generated at a single GNSS station. In short, by applying 3-D Zernike functions for modeling the 3-D wet refractivity field, the SWDs take the form of Radon transform, the inverse process of which is endogenously ill-posed and can be regularized by adding sufficient additional a priori information that we proposed in this work. The feasibility of our method has been demonstrated by a simulation. Although this method is heavy in computation, its major advantages are that no GNSS networks are required as in GNSS tomography

and it can be implemented in parallel with several GNSS stations. Moreover, compared to the conventional model of SWDs, this new method could give more physical information about the atmospheric conditions as both nonturbulent and turbulent motions are taken into account.

Although the method that we proposed is mainly for a standalone GNSS station, it can also be adapted to GNSS networks. There are two ways to do this. The first way is to directly apply our standalone method to every single station in the network. It can be expected that those 3-D wet refractivity fields that are retrieved from each station may overlap, leading to an additional control on the reconstructed 3-D wet refractivity field over the span of the atmosphere covered by the network. In the second way, the set of 3-D Zernike functions must be replaced by a more suitable spectral representation (with respect to space), which is tailored to the network, e.g., an empirical orthogonal function (EOF) basis. Similar studies on oceanography have already been carried out using this approach, e.g., for modeling sea surface topography [74]. The usual GNSS tomography framework with discrete voxels is an alternative to the EOFs since it is essentially a set of function bases with 1 inside each voxel and 0 outside the voxel. Meanwhile, the same a priori information (correlations of the modeled wet refractivity field in time and space) proposed in our study can be kept as it provides additional physical information regardless of the model representations. This information can be helpful, e.g., to reduce the number of stations required in a GNSS network when using the GNSS tomography technique.

At this moment, only simulation results are presented in this work. Therefore, it is natural to come to the question: is this method applicable to real datasets? The answer is carefully *not yet but probably soon* if the two kinds of the a priori information that we proposed in this work are shortly available, i.e., the a priori information on SWDs and model parameters (or wet refractivity field). In practice, the a priori information on SWDs could be obtained from the spatial/temporal covariance functions of SE series based on the SWDs generated at the GNSS stations of concern [53].

However, it is tricky to give the a priori information on model parameters, i.e., the Kaula-like rule. It is suggested that a general way to derive a realistic Kaula-like rule is to perform a spectral analysis of the wet refractivity field within the spatiotemporal scale that is of concern. Unfortunately, so far to our best knowledge, no such studies are available. The most promising way is using NWM products. However, the resolution of the present NWM products is too low to apply to a relatively smaller area, e.g., 2~5 km (required in our case) versus about 30 km by ERA5. Nevertheless, high-resolution NWMs are being developed (e.g., AROME-France and ARPEGE models in Europe [75], [76]) and it can be expected that the resolution of NWM products will be continuously improved over the globe. Once a fine resolution of NWM products is achieved, e.g., 2~5 km in space, a more realistic Kaula-like rule can be derived, as well as the covariance function of the wet refractivity field.

In addition, the SWDs that are currently retrieved from GNSS with mapping functions and horizontal gradients are too

coarse for us as this conventional model cannot represent the atmospheric conditions/processes on relatively smaller scales (e.g., from hundreds of meters to several kilometers in space and several minutes in time). The data coverage overhead of a standalone GNSS station is also limited by the nearly repetitive satellite tracks. Nevertheless, high-spatiotemporal-resolution data coverage is coming soon with multiconstellations, especially the low Earth orbit (LEO) constellations. It has been shown in many previous studies that the upcoming LEO satellites will significantly improve the coverage and the geometry of observations overhead a standalone GNSS station with the so-called LEO augmented GNSS technique (LeGNSS) (see [77], [78]). Until then, SWDs with a higher spatiotemporal resolution can be retrieved with LeGNSS. This would be of great help for applying our method to resolve the 3-D wet refractivity field on a local scale as these SWDs could give a better representation of the real complex weather conditions and atmospheric processes. Therefore, our contribution can be considered as the first step to see whether the proposed method was feasible and robust from the viewpoint of mathematics with ideal conditions in the simulation.

It should be pointed out that the results from real datasets may be different from the ones presented here. This is because our simulation is based on a priori covariance functions, which are unsighted to the means in the considered quantities. We here simply assume that the mean of the fluctuating component ε_w of the wet refractivity field is zero.

However, this is not always true. As a result, the results of our simulation can only be considered as perturbations $\delta\varepsilon_w$ superimposed on an unknown "mean" (or to say it better, a background value) $\bar{\varepsilon}_w$, also a potentially fluctuating component of the wet refractivity field. In practice, this "hidden" mean part must be calibrated using observations from other techniques, e.g., radiosonde, when applying our method to real datasets. The results of modeling $\delta\varepsilon_w$ from real datasets and our simulation are only comparable if $\bar{\varepsilon}_w$ is defined in such a way that the mean of $\delta\varepsilon_w$ is zero. The derivation of a physically sound $\bar{\varepsilon}_w$ is by itself another interesting topic and needs to be further investigated. However, it is out of the scope of this work.

In our future work, we will consider simulating the 4-D wet refractivity field, i.e., with the addition of time evolution. The inclusion of time evolution allows us to describe critical atmospheric processes such as deep convection and cloud formation. The introduction of time variability is less problematic from a mathematical point of view as most of the ill-posedness lies with the Radon transform in space. The time scale has not yet been considered, but we infer that it should take a resolution of at least 30 min to accumulate sufficient observations for constraining the model. In that case, the correlation time of up to four days for GNSS-derived SWDs (see Section II) should be included as another a priori information for time-varying parameters. Besides, the Kaula-like rule needs to be reconsidered according to the degree of the orthonormal functions used to represent the temporal variations.

However, the number of unknowns to be solved will increase dramatically by introducing the time variability
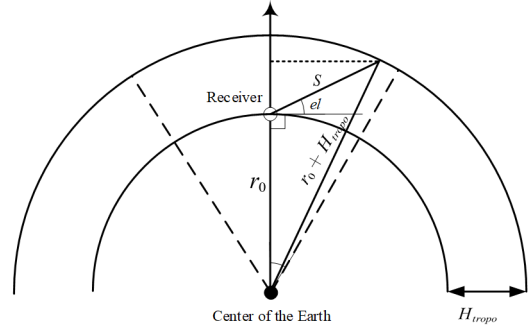

Fig. 16. Geometry of a ray path launching from a single station at the elevation angle *el*.

[see (3)]. The corresponding linear systems with a tremendous number of unknowns (up to tens of thousands) will have to be solved with the help of a highly parallel supercomputer with sufficient memory. Taking the 3-D case in this work as a milestone, a fully mature 4-D model with time evolution involved will eventually be accomplished as we move forward in the direction mentioned above.

APPENDIX

Assuming that the ray path is limited to a certain azimuthally fixed vertical plane, the 2-D geometry of a ray path S launching at an elevation angle *el* from a single station is shown in Fig. 16. The delay $\overline{\text{SWD}}$ therefore can be computed as

$$\overline{\text{SWD}} = N_w^0 \cdot \int_s \exp\left(-\frac{r - r_0}{H_w}\right) ds$$
$$= N_w^0 \cdot \int_0^S \exp\left(-\frac{s \cdot \sin(el)}{H_w}\right) ds$$
$$= -\frac{N_w^0 H_w}{\sin(el)}\left[\exp\left(-\frac{S \cdot \sin(el)}{H_w}\right) - 1\right]. \quad (23)$$

The ray path S usually can be obtained by implementing the so-called ray-tracing, and however, here for simplicity, we take the ray path as a straight line. Thereby, S can be derived from a given *el* based on the geometry illustrated in Fig. 16 as

$$(r_0 + S \cdot \sin(el))^2 + (S \cdot \cos(el))^2 = \left(r_0 + H_{\text{tropo}}\right)^2 \quad (24)$$

$$S = \frac{-2r_0 \sin(el) + \sqrt{4r_0^2 \sin^2(el) + 4 \cdot \left(2r_0 \cdot H_{\text{tropo}} + H_{\text{tropo}}^2\right)}}{2} \quad (25)$$

where $H_{\text{tropo}} = 16.5$ km is the height of the tropopause in our case. The other parameters can be found in the context of Section III.

For the other delay δSWD in (8), we have

$$\delta\text{SWD} = N_w^0 \cdot \int_0^S \exp\left(-\frac{s \cdot \sin(el)}{H_w}\right) \cdot \varepsilon_w ds. \quad (26)$$

By changing the variable of the integration $s = \mu \cdot S$, i.e., $ds = S \cdot d\mu$, we have the integral over the interval [0, 1] that follows the limitation of r ($0 \leq r \leq 1$) in the radial polynomials $R_n^l(r)$ of 3-D Zernike functions. Thereby, together with 3-D Zernike

functions in (4), (26) can be rewritten as

$$\delta\text{SWD} = N_w^0 \cdot \sum_{n=0}^{n_{\max}} \sum_{l=0}^{n} \sum_{m=0}^{l} \int_0^1 \exp\left(-\frac{\mu S \cdot \sin(el)}{H_w}\right) R_n^l(\mu)d\mu$$
$$\cdot Y_l^m(\theta, \lambda) \cdot p_{nl}^m. \tag{27}$$

Note that only the radial polynomials $R_n^l(\mu)$ and the exponential function in (27) depend on the variable of integration. Considering that the ansatz in (7) and the radial polynomials $R_n^l(\mu)$ take the form [64]

$$R_n^l(\mu) = \sum_{v=0}^{k=(n-l)/2} q_{kl}^v \cdot \mu^{2v+l} \tag{28}$$

the definite integral in (27) can be derived as

$$\int_0^1 \exp\left(-\frac{\mu S \cdot \sin(el)}{H_w}\right) R_n^l(\mu)d\mu$$
$$= \sum_{v=0}^{k=(n-l)/2} q_{kl}^v \int_0^1 \exp\left(-\frac{\mu S \cdot \sin(el)}{H_w}\right) \mu^{2v+l} d\mu$$
$$= \sum_{v=0}^{k=(n-l)/2} q_{kl}^v \left[-\frac{1}{a^{2v+l+1}} \Gamma(2v+l+1, a\mu) \right]\Bigg|_0^1$$
$$= \sum_{v=0}^{k=(n-l)/2} q_{kl}^v \cdot \frac{l}{a^{2v+l+1}} \gamma(2v+l+1, a). \tag{29}$$

We let $a = S \cdot \sin(el)/H_w$ in (7). Here, Γ and γ denote the upper and lower incomplete Gamma functions, respectively. By substituting (29) into (27), (10) is derived.

ACKNOWLEDGMENT

REFERENCES

[1] F. K. Brunner, "The effects of atmospheric turbulence on telescopic observations," *Bull. Géodésique*, vol. 56, no. 4, pp. 341–355, Dec. 1982, doi: 10.1007/bf02525733.

[2] V. Raizer, *Remote Sensing of Turbulence*, 1st ed. Boca Raton, FL, USA: CRC Press, 2022.

[3] R. E. Good, R. R. Beland, E. A. Murphy, J. H. Brown, and E. M. Dewan, "Atmospheric models of optical turbulence," in *Modeling of the Atmosphere*, vol. 928. Bellingham, WA, USA: SPIE, 1988, p. 165, doi: 10.1117/12.975626.

[4] J. Barriot and P. Feng, "Beyond mapping functions and gradients," in *Geodetic Sciences—Theory, Applications and Recent Developments*, vol. 32. London, U.K.: IntechOpen, Jul. 2021, pp. 137–144, doi: http://dx.doi.10.5772/intechopen.96982. [Online]. Available: http://dx.doi.org/10.5772/intechopen.96982

[5] S. Halsig, T. Artz, A. Iddink, and A. Nothnagel, "Using an atmospheric turbulence model for the stochastic model of geodetic VLBI data analysis," *Earth, Planets Space*, vol. 68, no. 1, pp. 1–14, Dec. 2016, doi: 10.1186/s40623-016-0482-5.

[6] T. Nilsson and R. Haas, "Impact of atmospheric turbulence on geodetic very long baseline interferometry," *J. Geophys. Res., Solid Earth*, vol. 115, no. B3, pp. 1–11, Mar. 2010, doi: 10.1029/2009jb006579.

[7] S. C. Herring, N. Christidis, A. Hoell, J. P. Kossin, C. J. Schreck, and P. A. Stott, "Explaining extreme events of 2016 from a climate perspective," *Bull. Amer. Meteorol. Soc.*, vol. 99, no. 1, pp. S1–S157, Jan. 2018, doi: 10.1175/bams-explainingextremeevents2016.1.

[8] J. Vaquero-Martínez and M. Antón, "Review on the role of GNSS meteorology in monitoring water vapor for atmospheric physics," *Remote Sens.*, vol. 13, no. 12, p. 2287, Jun. 2021, doi: 10.3390/rs13122287.

[9] M. Bevis, S. Businger, T. A. Herring, C. Rocken, R. A. Anthes, and R. H. Ware, "GPS meteorology: Remote sensing of atmospheric water vapor using the global positioning system," *J. Geophys. Res., Atmos.*, vol. 97, no. D14, pp. 15787–15801, Oct. 1992, doi: 10.1029/92jd01517.

[10] J. Van Baelen et al., "On the relationship between water vapour field evolution and the life cycle of precipitation systems," *Quart. J. Roy. Meteorol. Soc.*, vol. 137, no. S1, pp. 204–223, Jan. 2011, doi: 10.1002/qj.785.

[11] W. Zhang et al., "Multiscale variations of precipitable water over China based on 1999–2015 ground-based GPS observations and evaluations of reanalysis products," *J. Climate*, vol. 31, no. 3, pp. 945–962, Feb. 2018, doi: 10.1175/jcli-d-17-0419.1.

[12] M. Troller, A. Geiger, E. Brockmann, J.-M. Bettems, B. Bürki, and H.-G. Kahle, "Tomographic determination of the spatial distribution of water vapor using GPS observations," *Adv. Space Res.*, vol. 37, no. 12, pp. 2211–2217, Jan. 2006, doi: 10.1016/j.asr.2005.07.002.

[13] Y. Yao and Q. Zhao, "Maximally using GPS observation for water vapor tomography," *IEEE Trans. Geosci. Remote Sens.*, vol. 54, no. 12, pp. 7185–7196, Dec. 2016, doi: 10.1109/TGRS.2016.2597241.

[14] Z. Adavi and M. Mashhadi-Hossainali, "4D tomographic reconstruction of the tropospheric wet refractivity using the concept of virtual reference station, case study: Northwest of Iran," *Meteorol. Atmos. Phys.*, vol. 126, nos. 3–4, pp. 193–205, Nov. 2014, doi: 10.1007/s00703-014-0342-4.

[15] S. Haji-Aghajany, Y. Amerian, and S. Verhagen, "B-spline function-based approach for GPS tropospheric tomography," *GPS Solutions*, vol. 24, no. 3, pp. 1–12, Jul. 2020, doi: 10.1007/s10291-020-01005-x.

[16] A. Flores, G. Ruffini, and A. Rius, "4D tropospheric tomography using GPS slant wet delays," *Annales Geophysicae*, vol. 18, no. 2, pp. 223–234, Feb. 2000, doi: 10.1007/s005850050025.

[17] S. Song, W. Zhu, J. Ding, and J. Peng, "3D water-vapor tomography with Shanghai GPS network to improve forecasted moisture field," *Chin. Sci. Bull.*, vol. 51, no. 5, pp. 607–614, Mar. 2006, doi: 10.1007/s11434-006-0607-5.

[18] M. Bender et al., "Development of a GNSS water vapour tomography system using algebraic reconstruction techniques," *Adv. Space Res.*, vol. 47, no. 10, pp. 1704–1720, May 2011, doi: 10.1016/j.asr.2010.05.034.

[19] W. Rohm, K. Zhang, and J. Bosy, "Limited constraint, robust Kalman filtering for GNSS troposphere tomography," *Atmos. Meas. Techn.*, vol. 7, no. 5, pp. 1475–1486, May 2014, doi: 10.5194/amt-7-1475-2014.

[20] W. Zhang et al., "Rapid troposphere tomography using adaptive simultaneous iterative reconstruction technique," *J. Geodesy*, vol. 94, no. 8, pp. 1–12, Aug. 2020, doi: 10.1007/s00190-020-01386-4.

[21] H. Hersbach et al., "The ERA5 global reanalysis," *Quart. J. Roy. Meteorol. Soc.*, vol. 146, no. 730, pp. 1999–2049, Jul. 2020, doi: 10.1002/qj.3803.

[22] T. Foken, *Springer Handbook of Atmospheric Measurements*, 1st ed. Cham, Switzerland: Springer, 2021.

[23] R. A. Anthes, "Exploring Earth's atmosphere with radio occultation: Contributions to weather, climate and space weather," *Atmos. Meas. Techn.*, vol. 4, no. 6, pp. 1077–1103, Jun. 2011, doi: 10.5194/amt-4-1077-2011.

[24] J. Barriot, J. Serafini, and L. Sichoix, "Estimating the 3D time variable water vapor contents of the troposphere from a single GNSS receiver," in *Proc. Int. Conf. Earth Obs. Soc. Impacts (ICEO&SI)*, 2013, pp. 3–8.

[25] J. Radon, "On the determination of functions from their integral values along certain manifolds," *IEEE Trans. Med. Imag.*, vol. 5, no. 4, pp. 170–176, Dec. 1986, doi: 10.1109/TMI.1986.4307775.

[26] F. Colonna, G. Easley, K. Guo, and D. Labate, "Radon transform inversion using the Shearlet representation," *Appl. Comput. Harmon. Anal.*, vol. 29, no. 2, pp. 232–250, Sep. 2010, doi: 10.1016/j.acha.2009.10.005.

[27] M. Benna, J.-P. Barriot, and W. Kofman, "A priori information required for a two or three dimensional reconstruction of the internal structure of a comet nucleus (consert experiment)," *Adv. Space Res.*, vol. 29, no. 5, pp. 715–724, Mar. 2002, doi: 10.1016/s0273-1177(02)00009-1.

[28] J.-P. Barriot, W. Kofman, A. Herique, S. Leblanc, and A. Portal, "A two dimensional simulation of the CONSERT experiment (radio tomography of comet Wirtanen)," *Adv. Space Res.*, vol. 24, no. 9, pp. 1127–1138, Jan. 1999, doi: 10.1016/s0273-1177(99)80206-3.

[29] A. N. Kolmogorov, "Dissipation of energy in locally isotropic turbulence," *Proc. Math. Phys. Sci.*, vol. 434, no. 1890, pp. 15–17, 1991. Accessed: Jun. 17, 2024. [Online]. Available: http://www.jstor.org/stable/51981

[30] G. I. Taylor, "The spectrum of turbulence," *Proc. Roy. Soc. Lond. A, Math. Phys. Eng. Sci.*, vol. 164, no. 919, pp. 476–490, Feb. 1938, doi: 10.1098/rspa.1938.0032.

[31] S. Williams, Y. Bock, and P. Fang, "Integrated satellite interferometry: Tropospheric noise, GPS estimates and implications for interferometric synthetic aperture radar products," *J. Geophys. Res., Solid Earth*, vol. 103, no. B11, pp. 27051–27067, Nov. 1998.

[32] V. I. Tatarskii, *The Effects of the Turbulent Atmosphere on Wave Propagation*. Springfield, VA, USA: Israel Program for Scientific Translations, 1971.

[33] L. P. Gradinarsky and P. Jarlemark, "Ground-based GPS tomography of water vapor: Analysis of simulated and real data," *J. Meteorol. Soc. Japan. Ser. II*, vol. 82, no. 1B, pp. 551–560, 2004, doi: 10.2151/jmsj.2004.551.

[34] T. Nilsson and L. Gradinarsky, "Water vapor tomography using GPS phase observations: Simulation results," *IEEE Trans. Geosci. Remote Sens.*, vol. 44, no. 10, pp. 2927–2941, Oct. 2006, doi: 10.1109/TGRS.2006.877755.

[35] R. N. Treuhaft and G. E. Lanyi, "The effect of the dynamic wet troposphere on radio interferometric measurements," *Radio Sci.*, vol. 22, no. 2, pp. 251–265, Mar. 1987, doi: 10.1029/RS022i002p00251.

[36] S. Schön and F. K. Brunner, "Atmospheric turbulence theory applied to GPS carrier-phase data," *J. Geodesy*, vol. 82, no. 1, pp. 47–57, Jan. 2008, doi: 10.1007/s00190-007-0156-y.

[37] A. Romero-Wolf, C. S. Jacobs, and J. T. Ratcliff, "Effects of tropospheric spatio-temporal correlated noise on the analysis of space geodetic data," in *Proc. IVS Gen. Meeting*, 2012, no. 1941, pp. 231–235. [Online]. Available: http://ivscc.gsfc.nasa.gov/publications/gm2012/Romero-Wolf.pdf

[38] A. Pany, J. Böhm, D. Macmillan, H. Schuh, T. Nilsson, and J. Wresnik, "Monte Carlo simulations of the impact of troposphere, clock and measurement errors on the repeatability of VLBI positions," *J. Geodesy*, vol. 85, no. 1, pp. 39–50, Jan. 2011, doi: 10.1007/s00190-010-0415-1.

[39] T. R. Emardson and P. O. J. Jarlemark, "Atmospheric modelling in GPS analysis and its effect on the estimated geodetic parameters," *J. Geodesy*, vol. 73, no. 6, pp. 322–331, Jul. 1999, doi: 10.1007/s001900050249.

[40] S. Schön and F. K. Brunner, "A proposal for modelling physical correlations of GPS phase observations," *J. Geodesy*, vol. 82, no. 10, pp. 601–612, Oct. 2008, doi: 10.1007/s00190-008-0211-3.

[41] G. Kermarrec and S. Schön, "On the Mátern covariance family: A proposal for modeling temporal correlations based on turbulence theory," *J. Geodesy*, vol. 88, no. 11, pp. 1061–1079, Nov. 2014, doi: 10.1007/s00190-014-0743-7.

[42] S. Halsig, T. Artz, J. Leek, and A. Nothnagel, "VLBI analyses using covariance information from turbulence models," in *Proc. Int. VLBI Service Geodesy Astrometry Gen. Meeting*, 2014, pp. 272–276.

[43] C. Faccani, R. Ferretti, R. Pacione, T. Paolucci, F. Vespe, and L. Cucurull, "Impact of a high density GPS network on the operational forecast," *Adv. Geosci.*, vol. 2, pp. 73–79, Mar. 2005, doi: 10.5194/adgeo-2-73-2005.

[44] Q. Zhao, Y. Yao, and W. Yao, "GPS-based PWV for precipitation forecasting and its application to a typhoon event," *J. Atmos. Solar-Terrestrial Phys.*, vol. 167, pp. 124–133, Jan. 2018, doi: 10.1016/j.jastp.2017.11.013.

[45] G. Guerova et al., "Review of the state of the art and future prospects of the ground-based GNSS meteorology in Europe," *Atmos. Meas. Techn.*, vol. 9, no. 11, pp. 5385–5406, Nov. 2016, doi: 10.5194/amt-9-5385-2016.

[46] S. Bonafoni, R. Biondi, H. Brenot, and R. Anthes, "Radio occultation and ground-based GNSS products for observing, understanding and predicting extreme events: A review," *Atmos. Res.*, vol. 230, Dec. 2019, Art. no. 104624, doi: 10.1016/j.atmosres.2019.104624.

[47] T. Nilsson and G. Elgered, "Long-term trends in the atmospheric water vapor content estimated from ground-based GPS data," *J. Geophys. Res., Atmos.*, vol. 113, no. D19, pp. 1–12, Oct. 2008, doi: 10.1029/2008jd010110.

[48] Z. Baldysz, G. Nykiel, A. Araszkiewicz, M. Figurski, and K. Szafranek, "Comparison of GPS tropospheric delays derived from two consecutive EPN reprocessing campaigns from the point of view of climate monitoring," *Atmos. Meas. Techn.*, vol. 9, no. 9, pp. 4861–4877, Sep. 2016, doi: 10.5194/amt-9-4861-2016.

[49] C. Champollion, F. Masson, J. Van Baelen, A. Walpersdorf, J. Chéry, and E. Doerflinger, "GPS monitoring of the tropospheric water vapor distribution and variation during the 9 September 2002 torrential precipitation episode in the Cévennes (Southern France)," *J. Geophys. Res., Atmos.*, vol. 109, no. D24, pp. 1–15, Dec. 2004, doi: 10.1029/2004jd004897.

[50] H. Brenot et al., "Preliminary signs of the initiation of deep convection by GNSS," *Atmos. Chem. Phys.*, vol. 13, no. 11, pp. 5425–5449, Jun. 2013, doi: 10.5194/acp-13-5425-2013.

[51] V. Graffigna, M. Hernández-Pajares, F. Azpilicueta, and M. Gende, "Comprehensive study on the tropospheric wet delay and horizontal gradients during a severe weather event," *Remote Sens.*, vol. 14, no. 4, p. 888, Feb. 2022.

[52] L. Morel et al., "Validity and behaviour of tropospheric gradients estimated by GPS in Corsica," *Adv. Space Res.*, vol. 55, no. 1, pp. 135–149, Jan. 2015, doi: 10.1016/j.asr.2014.10.004.

[53] F. Zhang, J.-P. Barriot, G. Xu, and M. Hopuare, "Modeling the slant wet delays from one GPS receiver as a series expansion with respect to time and space: Theory and an example of application for the tahiti island," *IEEE Trans. Geosci. Remote Sens.*, vol. 58, no. 11, pp. 7520–7532, Nov. 2020, doi: 10.1109/TGRS.2020.2975458.

[54] M. Vennebusch, S. Schön, and U. Weinbach, "Temporal and spatial stochastic behaviour of high-frequency slant tropospheric delays from simulations and real GPS data," *Adv. Space Res.*, vol. 47, no. 10, pp. 1681–1690, May 2011, doi: 10.1016/j.asr.2010.09.008.

[55] W. M. Kaula and R. E. Street, *Theory of Satellite Geodesy: Applications of Satellites to Geodesy*, vol. 20, 1st ed. Waltham, MA, USA: Blaisdell, 1966.

[56] A. Broman, *Introduction to Partial Differential Equations From Fourier Series to Boundary-Value Problems*, 1st ed. New York, NY, USA: Dover, 1970.

[57] W. M. Kaula, "Determination of the Earth's gravitational field," *Rev. Geophysics*, vol. 1, no. 4, pp. 507–551, Nov. 1963, doi: 10.1029/rg001i004p00507.

[58] W. M. Kaula, "Statistical and harmonic analysis of gravity," *J. Geophys. Res.*, vol. 64, no. 12, pp. 2401–2421, Dec. 1959, doi: 10.1029/jz064i012p02401.

[59] R. H. Rapp and N. K. Pavlis, "The development and analysis of geopotential coefficient models to spherical harmonic degree 360," *J. Geophys. Res., Solid Earth*, vol. 95, no. B13, pp. 21885–21911, Dec. 1990, doi: 10.1029/jb095ib13p21885.

[60] R. S. Nerem, C. Jekeli, and W. M. Kaula, "Gravity field determination and characteristics: Retrospective and prospective," *J. Geophys. Res., Solid Earth*, vol. 100, no. B8, pp. 15053–15074, Aug. 1995, doi: 10.1029/94jb03257.

[61] W. M. Kaula, "The investigation of the gravitational fields of the Moon and planets with artificial satellites," *Adv. Sp. Sci. Technol.*, vol. 5, pp. 210–230, Jul. 1963.

[62] J. Saastamoinen, "Contributions to the theory of atmospheric refraction: Part II. Refraction corrections in satellite geodesy," *Bull. Géodésique*, vol. 107, no. 1, pp. 13–34, Mar. 1973.

[63] F. S. Solheim, J. Vivekanandan, R. H. Ware, and C. Rocken, "Propagation delays induced in GPS signals by dry air, water vapor, hydrometeors, and other particulates," *J. Geophys. Res., Atmos.*, vol. 104, no. D8, pp. 9663–9670, Apr. 1999, doi: 10.1029/1999jd900095.

[64] M. Novotni and R. Klein, "3D Zernike descriptors for content based shape retrieval," in *Proc. 8th ACM Symp. Solid Modeling Appl.*, Jun. 2003, pp. 216–225, doi: 10.1145/781606.781639.

[65] R. J. Mathar, "Zernike basis to Cartesian transformations," *Serbian Astronomical J.*, no. 179, pp. 107–120, 2009, doi: 10.2298/saj0979107m.

[66] V. Lakshminarayanan and A. Fleck, "Zernike polynomials: A guide: [Journal of modern optics, vol. 58, Nos. 7–8, 10 April–10 May 2011, 545–561]," *J. Mod. Opt.*, vol. 58, no. 18, p. 1678, Oct. 2011, doi: 10.1080/09500340.2011.633763.

[67] P. Bolgiani et al., "Wind kinetic energy climatology and effective resolution for the ERA5 reanalysis," *Climate Dyn.*, vol. 59, nos. 3–4, pp. 737–752, Aug. 2022, doi: 10.1007/s00382-022-06154-y.

[68] J. Y. N. Cho, R. E. Newell, and J. D. Barrick, "Horizontal wavenumber spectra of winds, temperature, and trace gases during the Pacific exploratory missions: 2. Gravity waves, quasi-two-dimensional turbulence, and vortical modes," *J. Geophys. Res., Atmos.*, vol. 104, no. D13, pp. 16297–16308, Jul. 1999, doi: 10.1029/1999jd900068.

[69] A. Sneppen, "The power spectrum of climate change," *Eur. Phys. J. Plus*, vol. 137, no. 5, pp. 1–14, May 2022, doi: 10.1140/epjp/s13360-022-02773-w.

[70] J. L. Davis, "The effect of turbulence on atmospheric gradient parameters estimated from ground-based radiometric and space geodetic measurements," *Geophys. Res. Lett.*, vol. 19, no. 21, pp. 2183–2186, Nov. 1992, doi: 10.1029/92gl02510.

[71] J. Bouman, "Quality assessment of geopotential models by means of redundancy decomposition," *DEOS Prog. Lett.*, vol. 97, no. 1, pp. 49–54, 1997.

[72] M. Vennebusch and S. Schön, "Generation of slant tropospheric delay time series based on turbulence theory," in *Proc. Int. Assoc. Geodesy Symposia*, vol. 136, 2012, pp. 801–807.

[73] J. P. Barriot and G. Balmino, "Estimation of local planetary gravity fields using line of sight gravity data and an integral operator," *Icarus*, vol. 99, no. 1, pp. 202–224, Sep. 1992, doi: 10.1016/0019-1035(92)90183-8.

[74] C. Hwang, "Spectral analysis using orthonormal functions with a case study on the sea surface topography," *Geophys. J. Int.*, vol. 115, no. 3, pp. 1148–1160, Dec. 1993, doi: 10.1111/j.1365-246x.1993.tb01517.x.

[75] N. Fourrié et al., "AROME-WMED, a real-time mesoscale model designed for the HyMeX special observation periods," *Geosci. Model Develop.*, vol. 8, no. 7, pp. 1919–1941, Jul. 2015, doi: 10.5194/gmd-8-1919-2015.

[76] F. Bouyssel et al., "The 2020 global operational NWP data assimilation system at Météo-France," in *Data Assimilation for Atmospheric, Oceanic and Hydrologic Applications*, vol. 4, S. K. Park and L. Xu, Eds. Cham, Switzerland: Springer, 2020, pp. 645–664.

[77] X. Li et al., "LEO constellation-augmented multi-GNSS for rapid PPP convergence," *J. Geodesy*, vol. 93, no. 5, pp. 749–764, May 2019, doi: 10.1007/s00190-018-1195-2.

[78] H. Ge et al., "LEO enhanced global navigation satellite system (LeG-NSS): Progress, opportunities, and challenges," *Geo-Spatial Inf. Sci.*, vol. 25, no. 1, pp. 1–13, 2022, doi: 10.1080/10095020.2021.1978277.

Jean-Pierre Barriot received the Ph.D. degree in theoretical physics from the University of Montpellier, Montpellier, France, in 1987, and the Habilitation degree in space physics from the University of Toulouse, Toulouse, France, in 1997.

Since 2006, he has been a Distinguished Professor of geophysics with the University of French Polynesia, Faa'a, French Polynesia, and the Head of the Geodesy Observatory of Tahiti, a joint Geodetic Observatory of CNES, NASA, and UPF. He is also an Invited Professor with the University of Wuhan, Wuhan, China. His research interests include geophysics of the Earth and planets, Earth and planetary atmospheres, and orbitography.

Xianjie Li received the M.Sc. degree in geodesy from Wuhan University, Wuhan, China, in 2018. He is currently pursuing the Ph.D. degree in geophysics with the Geodesy Observatory of Tahiti, University of French Polynesia, Faa'a, French Polynesia.

His research interests include the study of GNSS precise point positioning technique and its application on mean sea level changes and meteorology.

Yidong Lou received the M.Sc. and Ph.D. degrees in geodesy engineering from Wuhan University, Wuhan, China, in 2004 and 2008, respectively.

He is currently a Professor with the GNSS Research Center, Wuhan University. His research findings have been successfully applied to the major project, "National Beidou Ground-Based Augmentation System Development and Construction," which has realized the wide-area real-time positioning accuracy of Beidou from meter level to centimeter level, supporting the innovative applications of a nationwide network service. His research interests include the theoretical methods and software of GNSS real-time high-precision data processing and meteorological applications.

Jingna Bai received the master's degree from the GNSS Research Center, Wuhan University, Wuhan, China, in 2022, where she is currently pursuing the Ph.D. degree in geodesy and survey engineering.

Her research interests include GNSS data processing and GNSS meteorology.

Weixing Zhang received the Ph.D. degree in geodesy and surveying engineering from Wuhan University, Wuhan, China, in 2016.

He is currently an Associate Professor with the GNSS Research Center, Wuhan University. His research interests include GNSS data processing and GNSS meteorology.